

Monitoring Wheat Powdery Mildew (*Blumeria graminis* f. sp. *tritici*) Using Multisource and Multitemporal Satellite Images and Support Vector Machine Classifier

ZHAO Jinling¹, DU Shizhou^{2*}, HUANG Linsheng¹

(1. National Engineering Research Center for Analysis and Application of Agro-Ecological Big Data, Anhui University, Hefei 230601, China; 2. Institute of Crops, Academy of Agricultural Sciences, Hefei 230031, China)

Abstract: Since powdery mildew (*Blumeria graminis* f. sp. *tritici*) mainly infects the foliar of wheat, satellite remote sensing technology can be used to monitor and assess it on a large scale. In this study, multisource and multitemporal satellite images were used to monitor the disease and improve the classification accuracy. Specifically, four Landsat-8 thermal infrared sensor (TIRS) and twenty MODerate-resolution imaging spectroradiometer (MODIS) temperature product (MOD11A1) were used to retrieve the land surface temperature (LST), and four Chinese Gaofen-1 (GF-1) wide field of view (WVF) images was used to identify the wheat-growing areas and calculate the vegetation indices (VIs). ReliefF algorithm was first used to optimally select the vegetation index (VIs) sensitive to wheat powdery mildew, spatial-temporal fusion between Landsat-8 LST and MOD11A1 data was performed using the spatial and temporal adaptive reflectance fusion model (STARFM). The Z-score standardization method was then used to unify the VIs and LST data. Four monitoring models were then constructed through a single Landsat-8 LST, multi-temporal Landsat-8 LSTs (SLST), cumulative MODIS LST (MLST) and the combination of cumulative Landsat-8 and MODIS LST (SMLST) using the Support Vector Machine (SVM) classifier, that were LST-SVM, SLST-SVM, MLST-SVM and SMLST-SVM. Four assessment indicators including user accuracy, producer accuracy, overall accuracy and Kappa coefficient were used to compare the four models. The results showed that, the proposed SMLST-SVM obtained the best identification accuracies. The overall accuracy and Kappa coefficient of the SMLST-SVM model had the highest values of 81.2% and 0.67, respectively, while they were respectively 76.8% and 0.59 for the SLST-SVM model. Consequently, multisource and multitemporal LSTs can considerably improve the differentiation accuracies of wheat powdery mildew.

Key words: wheat powdery mildew; GF-1; MODIS; Landsat-8; land surface temperature; support vector machine

CLC number: S435.121.4; TP79

Documents code: A

Article ID: SA202202009

Citation: ZHAO Jinling, DU Shizhou, HUANG Linsheng. Monitoring wheat powdery mildew (*Blumeria graminis* f. sp. *tritici*) using multisource and multitemporal satellite images and support vector machine classifier[J]. Smart Agriculture, 2022, 4(1): 17-28. (in English with Chinese abstract)

赵晋陵, 杜世州, 黄林生. 联合多源多时相卫星影像和支持向量机的小麦白粉病监测方法[J]. 智慧农业(中英文), 2022, 4(1): 17-28.

Received date: 2021-08-20

Foundation items: The Natural Science Foundation of China (31971789); The Natural Science Foundation of Anhui Province (2008085MF184)

Biography: ZHAO Jinling (1981—), male, Ph.D., associate professor, research interests: remote sensing-based crop disease monitoring. E-mail: zhaojl@ahu.edu.cn.

*Corresponding author: DU Shizhou (1982—), male, Ph.D., associate professor, research interest: smart agriculture. E-mail: dsz315@sina.com.

1 Introduction

Powdery mildew (*Blumeria graminis* f. sp. *tritici*) can occur at all stages of the wheat growth. It is a serious disease in some provinces of China, such as Sichuan, Guizhou, and Yunnan^[1]. In recent years, it has become more severe in the wheat-growing areas of Northeastern China, North China, and Northwestern China. When infected by the disease, some serious results will be caused such as early withering of leaves, decrease of panicle number, and decrease of 1000-grain weight. Generally, the disease can lead to a 5%–10% reduction in yield and when it is seriously infected, a more serious loss of more than 20% can occur^[2]. In view of the harmful effects on wheat production caused by the wheat powdery mildew, it is of great significance to improve the monitoring efficiency and accuracy. However, it is difficult for traditional in-situ sampling and random investigation methods to meet the needs of large-scale monitoring due to the limitations in terms of timeliness, economy, and accuracy^[3]. Fortunately, the modern information technology has facilitated the accurate and efficient identification of crop diseases to ensure food security^[4–6].

In recent years, the development of remote sensing technology has provided an important means for monitoring and forecasting large-scale wheat diseases and insect pests. It obtains crop information quickly, accurately and objectively. Many scholars have studied remote sensing-based monitoring of wheat diseases and insect pests by using ground-based, airborne and spaceborne remote sensing data. For example, Huang et al.^[7] showed that the photochemical reflectance index (PRI) was strongly correlated with wheat yellow rust and the coefficient of determination (R^2) could reach 0.97 for the PRI-based monitoring model. Zhang et al.^[8] built a discriminant model for wheat powdery mil-

dew severities by introducing continuous wavelet analysis based on the leaf-scale hyperspectral data. Luo et al.^[9] constructed a monitoring model of wheat aphid in two-dimensional feature space derived from the modified normalized difference water index (MNDWI) and land surface temperature (LST) based on Landsat-5 TM imagery, which had a high discriminant precision. Zheng et al.^[10] constructed a red edge disease stress index (REDSI) using three red-edge bands from Sentinel-2 satellite imagery for monitoring the stripe rust on winter wheat and got a satisfying result. The above studies showed that the spaceborne remote sensing images have greatly facilitated the monitoring and diagnosis of wheat diseases.

In previous studies, multispectral satellite images were adopted to investigate the large-scale disease occurrence. Since the rapid development of hyperspectral remote sensing technology, some studies on wheat powdery mildew had been explored using the hyperspectral data. More vegetation indices were derived from the hundreds of spectral bands of hyperspectral data. He et al.^[11] improved the monitoring accuracy of wheat powdery mildew severity by selecting suitable observation angles and developing a novel vegetation index (VI). Zhao et al.^[12] identified the powdery mildew severities of wheat leaves quantitatively on hyperspectral images and image segmentation techniques. Khan et al.^[13] detected the disease using a partial least-squares linear discrimination analysis and the combined optimal features (i.e., normalized difference texture indices (NDTIs) and VIs).

It can be found that the disease monitoring mainly depends on the vegetation changes between healthy and diseased wheat. Nevertheless, the commission and omission errors are usually caused due to the influences of other stress types such as

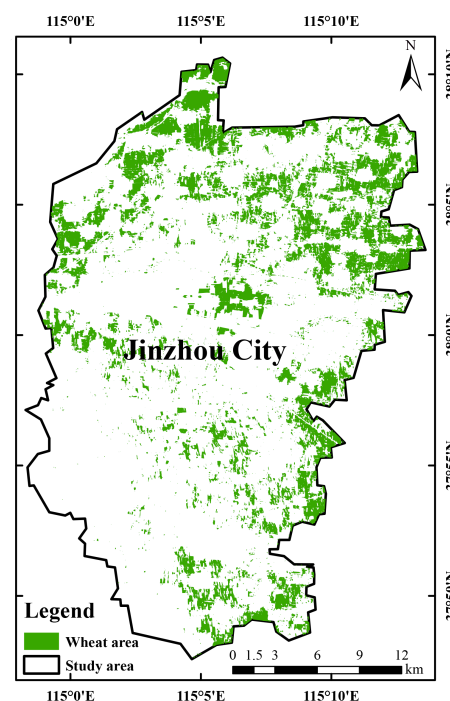
drought, inadequate nutrition, and other diseases. The incidence of wheat powdery mildew is involved in several affecting factors such as temperature, humidity and planting system. Considering the availability of temperature data of satellite images for large-scale monitoring, in this study, particular attention was given to the contribution of LST to the disease occurrence. As a key habitat factor, LST was included in the construction of monitoring model for the disease. LST remote sensing image was usually used in the previous monitoring of the disease^[14], but it has a cumulative effect on wheat powdery mildew. A single-phase LST image cannot accurately represent the disease occurrence condition during the whole growth period. The primary objective of this study was to explore the availability and feasibility to identify wheat powdery mildew using a combination of multisource and multitemporal spaceborne remote sensing imagery. More specifically, three types of satellite images were adopted to identify the wheat-planting areas and retrieve the LST. Single and multitemporal LSTs were input into the support vector machine (SVM) to compare the monitoring effects.

2 Materials and methods

2.1 Study area

The study area is located in Jinzhou City, Hebei province, China (114.97° — 115.20° E, 37.80° — 38.17° N) (Fig. 1). It has a warm-temperate continental monsoon climate, with a flat and open terrain. There is a significant seasonal variation of sun radiation. Wheat is one of the important grain crops and widely planted in this area. The critical periods of wheat growth range from April to May. Due to its flat terrain, appropriate climate conditions and relatively single planting structure, the region is

suitable for studying wheat powdery mildew using remote sensing technology^[15]. The historic statistical data also show that the occurrence frequency of wheat powdery mildew is high and hazard degree is serious^[16]. The wheat-planting areas were extracted by combining the elevation data and reflectance of the near-infrared (NIR) band of Chinese Gaofen-1 (GF-1) by using decision tree classification techniques (Fig. 1(b)). The extraction results were compared with the statistical data of Shijiazhuang City, which could fulfill the accuracy requirement of remote sensing-based crop extraction.



Note: This map is made based on the standard map with the approval number of Ji S [2020] 030 (冀 S【2020】030) downloaded from the standard map service website of the Ministry of Natural Resources of the People's Republic of China, and the boundaries of the base map has not been modified

Fig. 1 Spatial distribution of wheat-growing areas of the study area

2.2 Data collection and pre-processing

The data used in this study mainly were spaceborne remote sensing images and field survey data of wheat powdery mildew. In-situ experiments were

carried out on 27 and 28 May 2014 in the central areas of Jinzhou City. Several typical experimental regions were selected to collect the ground-truth data, where wheat was widely planted and wheat powdery mildew occurs frequently. A total of 69 valid data were acquired using the method presented by Yuan et al.^[17]. The wheat powdery mildew severities were specified according to the Rules for the investigation and forecast of wheat powdery mildew [B. graminis (DC.) Speer] (NY/T 613-2002). Firstly, the average severity D of diseased leaves for the colony leaves was calculated according to Equation (1). Then, the disease index I could be derived from Equation (2). The five levels were finally obtained according to Table 1. To increase the comparability of remote sensing-based disease monitoring, the five levels of severities were further divided into three levels of 0 (healthy), 1 (mild) and 2 (severe).

Table 1 Rules to determine the severity levels

Level	1	2	3	4	5
I	≤ 10	$10 < I \leq 20$	$20 < I \leq 30$	$30 < I \leq 40$	> 40

$$D = \frac{\sum(d_i \times l_i)}{L} \times 100 \quad (1)$$

where d_i is the value of eight severity levels, which is 1%, 5%, 10%, 20%, 40%, 60%, 80%, 100%; l_i is the number of diseased leaves for each level; L is the total number of investigated diseased leaves.

$$I = F \times D \times 100 \quad (2)$$

where F is the percentage of diseased leaf, which is ratio between the diseased leaves and total investigated leaves.

Multisource remote sensing data were composed of GF-1, Landsat-8 and MODerate-resolution imaging spectroradio-meter (MODIS) data products.

GF-1: Four scenes of GF-1 wide field of view (WFV) images were collected on 6, 17 and 26 May, and 7 June 2014, respectively, with the path/row

numbers of 3/93 and 4/92. There are four spectral bands for the GF-1 WFV sensor within the spectral range of 0.45–0.89 μm, with the spatial resolution of 16 m. The primary preprocessing procedures were performed including orthorectification, radiation calibration, atmospheric correction and image subsetting. The radiation brightness (L_e , W/(m²·sr·μm)) of a WFV image can be derived from Equation (3).

$$L_e = \frac{DN - offset}{gain} \quad (3)$$

where DN is the digital number of pixel. The absolute radiometric calibration coefficients (*gain* and *offset*) were derived from the China Center for Resources Satellite Data and Application (<http://www.cresda.com/CN/>). After finishing the radiometric calibration, the Fast Line-of-Sight Atmospheric Analysis of Spectral Hypercubes (FLAASH) module in ENVI 5.3 software was used to complete the atmospheric correction. The geometric correction was carried out using the second-order polynomial model with the accuracy of less than a pixel.

Landsat-8: The Landsat-8 operational land imager (OLI) data were used to estimate the land reflectance and the thermal infrared sensor (TIRS) data were used for retrieving the LST^[18]. Four scenes of cloud-free images were selected and their acquisition date was 4 April, 23 April, 15 May and 22 May 2014, respectively. They were preprocessed including accurate geometric correction and radiation correction.

MOD11A1 product: It provided daily per-pixel land surface temperature and emissivity (LST&E) with 1 km spatial resolution^[19]. A total of 20 images were obtained from the land processes distributed active archive center (LPDAAC) from 1 April to 27 May, 2014. The data were preprocessed using the MRT (MODIS Reprojection Tool).

2.3 Selection of vegetation indices

A total of eight VIs suitable for monitoring the

wheat powdery mildew were selected in this study based on the previous studies (Table 2).

Table 2 Selected vegetation indices in this study

Vegetation index	Abbreviation	Formula	
Simple Ratio Index ^[25]	SRI	$SRI = R_{NIR}/R_{Red}$	(4)
Normalized Difference Vegetation Index ^[26]	NDVI	$NDVI = (R_{NIR} - R_{Red})/(R_{NIR} + R_{Red})$	(5)
Normalized Difference Greenness Index ^[27]	NDGI	$NDGI = (R_{NIR} - R_{Green})/(R_{NIR} + R_{Green})$	(6)
Soil-Adjusted Vegetation Index ^[28]	SAVI	$SAVI = 1.5(R_{NIR} - R_{Red})/(R_{NIR} + R_{Red} + 0.5)$	(7)
Enhanced Vegetation Index ^[29]	EVI	$EVI = 2.5(R_{NIR} - R_{Red})/(R_{NIR} + 6R_{Red} - 7.5R_{Blue} + 1)$	(8)
Triangular Vegetation Index ^[30]	TVI	$TVI = 0.5[120(R_{NIR} - R_{Green}) - 200(R_{Red} - R_{Green})]$	(9)
Differential Vegetation Index ^[31]	DVI	$DVI = R_{NIR} - R_{Red}$	(10)
Structure Insensitive Pigment Index ^[32]	SIPI	$SIPI = (R_{NIR} - R_{Blue})/(R_{NIR} + R_{Blue})$	(11)

Note: R_{NIR} , R_{Red} , R_{Green} and R_{Blue} respectively refers to the spectral reflectance of near-infrared, red, green and blue bands of a GF-1 WFV image

To find out the most sensitive features, the ReliefF algorithm was used due to its advantages of dealing with multi-class classification problem and having no restrictions on the data types. A sample R was randomly taken from the training sample set each time, and then k nearest neighbor samples (near Hits) of R were found from the sample set of the same class as R , and k nearest neighbor samples (near Misses) were found from each sample set of different classes of R . The input features were ranked according to the weights from large to small. Then the correlation analysis was carried out for each feature and the combination with the smallest correlation coefficient was selected as the best combination for model construction. The superiority and efficiency have been illustrated in remote sensing-based classification and object recognition^[20-23]. Consequently, it was adopted to perform the feature selection, which gave different weights to the features in terms of the correlations between features and various disease samples^[24]. Specifically, according to the ReliefF algorithm, all the VI variables were sorted in descending order of weight, and eight VIs were selected with the weight of 0.075 as the threshold value. Then, the correlation analysis

among the selected features were conducted. When the correlation coefficient (r) of the feature owing the highest weight that was greater than 0.9, it was eliminated, and then that of the second highest weight with a high r was eliminated, and so on. In addition, there was a close relationship between the disease incidence and meteorological factors such as temperature, precipitation, humidity, etc. The changes of VIs calculated at different growth stages also affected the sensitivity to the disease. Considering the temporal features and accumulative effect of temperature, three VIs were finally selected, namely the SAVI on 26 May 2014 and the SIPI and EVI on 17 May 2014.

2.4 Estimation of LST

Two-channel nonlinear splitter algorithm was adopted to increase the information amount and reduce the influence of errors. The equation is shown as (12).

$$LST = b_0 + (b_1 + b_2 \frac{1 - \varepsilon}{\varepsilon} + b_3 \frac{\Delta\varepsilon}{\varepsilon^2}) \frac{T_i + T_j}{2} + \\ (b_4 + b_5 \frac{1 - \varepsilon}{\varepsilon} + b_6 \frac{\Delta\varepsilon}{\varepsilon^2}) \frac{T_i - T_j}{2} + \\ b_7 (T_i - T_j)^2 \quad (12)$$

where ε and $\Delta\varepsilon$ respectively represents the mean

and difference values of the two channels' emissivities depending on the land type and coverage; T_i and T_j are the observed brightness temperatures of the two channels; $b_i (i = 0, 1, 2, \dots, 7)$ is the simulation dataset of various coefficients which can be derived from laboratory data, atmospheric parameters and the atmospheric radiation transmission equation. In order to modify the calculation precision, the coefficient depends on the atmospheric water vapour column^[33]. Fig. 2 is the LST of 22 May 2014 retrieved from Landsat-8 TIRS image. In general, the LSTs of crop planting areas are lower than other regions. To calculate the land surface emissivity, the weighting method of vegetation coverage was adopted, which bases on the NDVI and vegetation coverage retrieved from the visible and NIR bands of Landsat-8 imagery^[34].

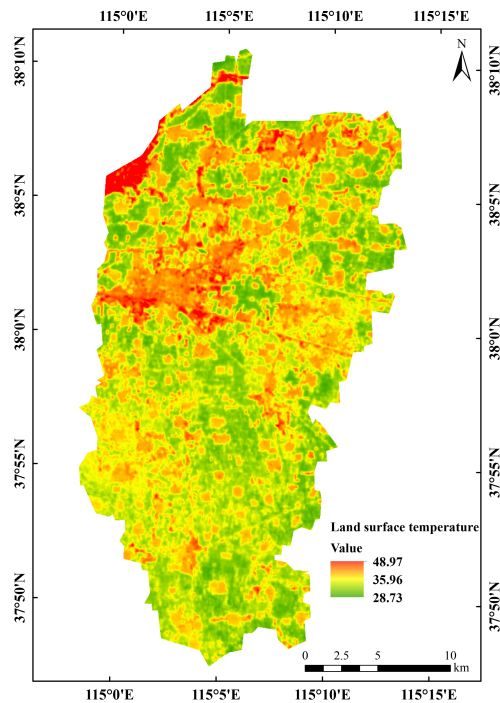


Fig. 2 The LST of Jinzhou estimated by the Landsat-8 TIRS image on 22 May 2014

The occurrence and development of wheat powdery mildew is a relatively long process during which the LST has a significant cumulative effect.

For example, temperature conditions which are favorable for wheat powdery mildew infection in early April will aggravate the disease. As a result, the disease at the end of May has a high correlation with previous LST. The Landsat-8 LST data at four growth stages were selected including the standing stage, jointing stage, flowering stage and milking stage, for the retrieval of LST and their summation SLST is shown in Equation (13).

$$\text{SLST} = \sum_{i=1}^4 \text{LST}_i - 20 \quad (13)$$

where SLST denotes the cumulative effect of multi-temporal Landsat-8 LST data; LST is calculated from a single Landsat-8 TIRS image; $i (1, 2, 3, 4)$ represents the four stages, and the 20 means the upper limit of temperature suitable for the incidence of wheat powdery mildew. Similarly, the summation of 20 MOD11A1 (MLST) can be also obtained according to the Equation (14).

$$\text{MLST} = \sum_{j=1}^{20} \text{LST}_j - 20 \quad (14)$$

2.5 Spatial-temporal fusion of MOD11A1 and Landsat-8 LST

Since the four Landsat-8 LST data cannot fully reflect the variation trend of LST during the whole wheat growth, the daily MOD11A1 was introduced. In order to obtain a data sequence that have enough spatial and temporal resolutions, the widely applied spatial and temporal adaptive reflectance fusion model (STARFM)^[35] was used to conduct the spatial-temporal fusion of Landsat-8 LST and MOD11A1. The algorithm ignores the spatial position registration and atmospheric correction errors, so the pixel values of low spatial resolution (LSR) remote sensing data at the moment t can be calculated using the weighted sum of that of high spatial resolution (HSR) data (Equation (15)).

$$C_t = \sum (F_t^i \times A_t^i) \quad (15)$$

where F_t^i is the pixel value of HSR data for the position i at the time t ; A_t^i shows the weight of coverage area for each pixel; C_t represents the pixel value of LSR data at the corresponding time.

The STARFM algorithm first obtains the MOD11A1 and Landsat-8 LST data and their deviation at the time t_k . The deviation is caused by the systematic errors and land cover changes. Meanwhile, the Landsat-8 LST of the time t_0 in accordance with MOD11A1 were predicted. The deviation remains constant as time changes was assumed, and the pixel values of Landsat-8 LST at the time t_0 are Equation (16).

$$\begin{aligned} \text{HSR}(x_i, y_i, t_0) &= \text{LSR}(x_i, y_i, t_0) + \\ &\quad \text{HSR}(x_i, y_i, t_k) - \text{LSR}(x_i, y_i, t_k) \end{aligned} \quad (16)$$

Considering the edge effect of pixels, a cloud-free pixel was selected in the moving window which was similar to the spectrum of central pixel when the pixel value was calculated. The calculating the central pixel value is shown as Equation (17).

$$\begin{aligned} \text{HSR}(x_{w/2}, y_{w/2}, t_0) &= \\ &\sum_{i=1}^w \sum_{j=1}^w \sum_{k=1}^w W_{ijk} \times (\text{LSR}(x_i, y_i, t_0) + \\ &\quad \text{HSR}(x_i, y_i, t_k) - \text{LSR}(x_i, y_i, t_k)) \end{aligned} \quad (17)$$

where w is the size of the moving window; $(x_{w/2}, y_{w/2})$ represents the position of central pixel; W_{ijk} denotes the weight coefficient of a pixel similar to the central pixel. The spectral distance weight, temporal distance weight, and spatial distance weight of a similar pixel were obtained in the window by a normalization method. The three weight coefficients were taken by referring to the study of Gao et al. in 2006^[35]. Four Landsat-8 LST (LST_i) and 20 MOD11A1 (LST_j) were used for the spatial-temporal fusion. The fusion data sequences were summed up as the SMLST in Equation (18).

$$\text{SMLST} = \sum_{i=1}^4 \text{LST}_i + \sum_{j=1}^{20} \text{LST}_j \quad (18)$$

2.6 Construction of monitoring models

Support vector machine (SVM) has the advantages of a simple structure, strong generalization ability, and high accuracy, which has been widely used in the classification of remote sensing images^[36]. The discriminant function of the model is shown as Equation (19).

$$f(x) = \text{sgn} \left(\sum_{x_i \in S_v} a_i y_i k(x_i, x) + b \right) \quad (19)$$

where a_i is the Lagrange multiplier; S_v is the support vector; x_i and y_i represent two kinds of support vectors; b is the threshold; $k(x_i, x)$ represents a positive definite kernel function which satisfies the Mercer theorem.

The Z-score method was used to standardize VIs and temperature data according to Equation (20) due to their different units. The training and validation datasets were divided using the ratio of 7:3. Four SVM-based models (LST-SVM, SLST-SVM, MLST-SVM and SMLST-SVM) were trained using the optimally selected three VIs. In addition to the VIs, these models were also involved in the Landsat-8 LST on 22 May (LST), four cumulative Landsat-8 LST data (SLST), 20 cumulative MOD11A1 (MLST) and cumulative spatial-temporal fusion LST combining Landsat-8 LST and MOD11A1 (SMLST), respectively. These models will explore a better application of remote sensing-based LST to the monitoring of wheat powdery mildew.

$$x' = (x - \mu) / \rho \quad (20)$$

where x' is the standardized data; μ is the mean of original data; ρ is the standard deviation.

3 Results and discussion

3.1 Validation of the monitoring results

The cross-validation was adopted to estimate the monitoring accuracies. As shown in Table 3,

four indicators, namely the user accuracy (UA), producer accuracy (PA), overall accuracy (OA) and Kappa coefficient (k) were used to assess the four SVM-based models. It could be seen that the SLST-SVM and SMLST-SVM achieved better classification performance. In terms of OA, the SMLST-SVM model obtained the best result, followed by the SLST-SVM and MLST-SVM models, while the LST-SVM model got the lowest value. The OAs of models indicated that the LST had a cumulative effect on the wheat powdery mildew infection. The k values of SMLST-SVM, MLST-SVM SLST-SVM and LST-SVM were 0.67, 0.54, 0.59 and 0.38, respectively, which also showed the similar trend with

OAs. From the perspective of UA, the ability of the four models to distinguish diseased and healthy wheat was strong. The differentiation ability of SLST-SVM and SMLST-SVM models for mild and severe wheat powdery mildew were significantly higher than that of LST-SVM model. The accuracies of MLST-SVM model were slightly lower than those of SLST-SVM and SMLST-SVM models, mainly due to the low spatial resolution of MOD11A1 data on the city scale. The above results show that the introduction of multi-temporal and cumulative LST can effectively improve the monitoring and identification of wheat powdery mildew severities.

Table 3 Comparison of the accuracies using the four monitoring models

Model	Confusion matrix			Accuracy assessment indicator			
	Healthy	Mild	Severe	User accuracy/%	Producer accuracy/%	Overall accuracy/%	k
LST-SVM	Healthy	14	7	0	66.7	63.6	
	Mild	8	25	4	83.8	65.8	63.8
	Severe	0	6	5	45.5	55.6	0.38
SLST-SVM	Healthy	14	7	0	66.7	82.4	
	Mild	3	32	2	86.5	74.4	76.8
	Severe	0	4	7	63.6	77.8	0.59
MLST-SVM	Healthy	15	6	0	71.4	88.2	
	Mild	2	32	3	86.5	71.1	73.9
	Severe	0	7	4	36.4	57.1	0.54
SMLST-SVM	Healthy	16	5	0	76.2	84.2	
	Mild	3	33	1	89.2	78.6	81.2
	Severe	0	4	7	63.6	87.5	0.67

Huang et al.^[37] identified wheat powdery mildew of the study area using 30 m-resolution Chinese HJ-1A/1B data to inverse LST and extract four-band reflectance data and build seven VIs. A combination method (GaborSVM) of SVM and Gabor wavelet features were proposed to obtain the OA of 86.7% that was higher than 81.2% of this study, but the OA of SVM-based method was 80% and lower than this study. The primary reason is that the spatial resolution of HJ-1B IRS is 300 m, but it is just 1000 m for MOD11A1. The comparison study

shows that spatial resolution of optical and thermal infrared satellite remote sensing images is an important factor of affect the accuracy of wheat powdery mildew.

3.2 Mapping of wheat powdery mildew

Based on multisource and multitemporal Landsat-8, GF-1 and MODIS data, three VIs of SIPI, SA-VI and EVI were optimally selected by the ReliefF algorithm and correlation analysis. The VIs and four temperature data of LST, SLST, MLST and

SMLST were respectively used to construct four monitoring models through the SVM, namely the LST-SVM, SLST-SVM, MLST-SVM and SMLST-SVM. For example, the severity distribution on 26 May 2014 in Jinzhou was shown in Fig. 3 using the SLST-SVM and SMLST-SVM models. The overall spatial distribution of wheat powdery mildew using

the two monitoring models were similar. Nevertheless, there were also some obvious differences as shown in the red boxes. It was more serious in the eastern part than in the western part of the study area. It was also obvious that the wheat powdery mildew mainly occurred in the areas where wheat was widely planted.

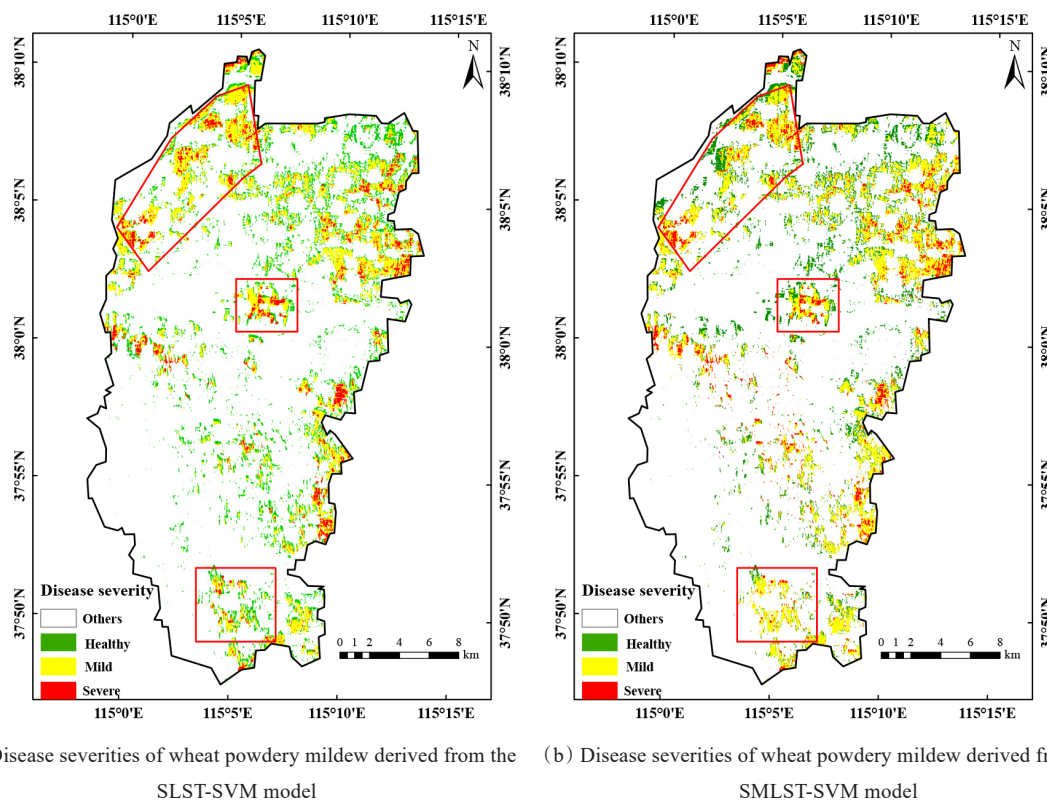


Fig. 3 Comparison of monitoring wheat powdery mildew by the SLST-SVM model and SMLST-SVM model

In the central regions where the ground-truth points were located, the monitoring results of the two models were also similar by visual observation. In the two figures, the distribution trends of wheat powdery mildew were both relatively concentrated. In comparison with the 32% of healthy samples, 55% of mild samples and 13% of severe samples for the in-situ investigation, they were 37%, 49% and 14% for the SLST-SVM model and 31%, 55% and 14% for SMLST-SVM model, respectively. It can be seen that the SMLST-SVM model had a bet-

ter result than SLST-SVM model.

3.3 Analysis of influence factors

Temperature is one of the key factors to affect the incidence of wheat powdery mildew, however, it is difficult and inaccurate to identify the disease in small and medium-sized regions, due to constraint of low spatial resolution of regular meteorological data. Ma et al.^[38] combined meteorological and remote sensing data to monitor wheat powdery mildew, because the distribution of meteorological stations was too sparse. The primary objective of this

study is to compare the relationship between LST and the disease severities of wheat powdery mildew. It can be found that different LST data have significant impact on the accuracies of the disease diagnosis. For example, in the retrieval of LST from Landsat-8 data, the two-channel nonlinear splitter used in this paper was more reliable than the single-channel method^[39]. The spatial resolution of Landsat-8 TIRS data and the temporal resolution of MOD11A1 data can both meet the requirements. Therefore, the combination and fusion of both the images were performed to acquire a better performance. The accumulated temperature and effective accumulated temperature are key factors to affect wheat powdery mildew^[40]. Multitemporal LST is better to show the temperature influence on the disease monitoring than a single one.

4 Conclusion

It is a progressive process for the occurrence of wheat powdery mildew, the cumulative effect must be considered with the disease development. To accurately identify the disease, multisource and multitemporal GF-1, Landsat-8 and MOD11A1 were jointly utilized at a city scale. The vegetation features and LSTs are simultaneously adopted to monitor the disease for improving the classification accuracy.

To find out the most sensitive vegetation features to wheat powdery mildew, four most important growth stages were selected including the standing stage, jointing stage, flowering stage and milking stage, which are also the criteria for selecting satellite images. Additionally, it has a progressive process for the disease incidence with the growth of wheat and changes of meteorological factors. As one of the most essential influencing factors, the accumulative effects in LSTs must be considered when identifying the disease. Landsat-8 TIRS has

high spatial resolution but low temporal resolution, however, it is quite contrary to MOD11A1. As a result, the STARFM was selected to perform the spatial-temporal fusion of both data. Four SVM models were respectively constructed through a single Landsat-8 LST (LST), multitemporal Landsat-8 LSTs (SLST), cumulative MODIS LST (MLST) and the combination of cumulative Landsat-8 and MODIS LST (SMLST).

The OA of LST-SVM model was improved by 13% using the four temporal LSTs. In addition, the Kappa coefficient also increased from 0.38 to 0.59, indicating that LST is a key habitat factor for the occurrence and development of wheat powdery mildew, due to a cumulative effect. On the other hand, the accuracies of MLST-SVM model were smaller than that of SLST-SVM and SMLST-SVM models, indicating that it is inappropriate to apply MOD11A1 data directly to the monitoring of wheat powdery mildew in a relatively small area. Conversely, the performance of SMLST-SVM is slightly better than that of SLST-SVM, indicating that the monitoring performance can be enhanced by using a combination and fusion of high-resolution spatial-temporal remote sensing data.

References :

- [1] ZHANG J, WANG N, YUAN L, et al. Discrimination of winter wheat disease and insect stresses using continuous wavelet features extracted from foliar spectral measurements[J]. Biosystems Engineering, 2017, 162: 20-29.
- [2] FENG W, SHEN W Y, HE L, et al. Improved remote sensing detection of wheat powdery mildew using dual-green vegetation indices[J]. Precision Agriculture, 2016, 17(5): 608-627.
- [3] GALLEGOS F J, KUSSUL N, SKAKUN S, et al. Efficiency assessment of using satellite data for crop area estimation in Ukraine[J]. International Journal of Applied Earth Observation and Geoinformation, 2014, 29: 22-30.
- [4] SETHY P K, BARPANDA N K, RATH A K, et al. Image processing techniques for diagnosing rice plant dis-

ease: A survey[J]. Procedia Computer Science, 2020, 167: 516-530.

[5] YANG C. Remote sensing and precision agriculture technologies for crop disease detection and management with a practical application example[J]. Engineering, 2020, 6(5): 528-532.

[6] ZHENG Q, YE H, HUANG W, et al. Integrating spectral information and meteorological data to monitor wheat yellow rust at a regional scale: A case study[J]. Remote Sensing, 2021, 13(2): ID 278.

[7] HUANG W J, LAMB D W, NIU Z, et al. Identification of yellow rust in wheat using in-situ spectral reflectance measurements and airborne hyperspectral imaging[J]. Precision Agriculture, 2007, 8(4-5): 187-197.

[8] ZHANG J C, PU R L, WANG J H, et al. Detecting powdery mildew of winter wheat using leaf level hyperspectral measurements[J]. Computers and Electronics in Agriculture, 2012, 85: 13-23.

[9] LUO J H, ZHAO C J, HUANG W J, et al. Discriminating wheat aphid damage degree using 2-dimensional feature space derived from Landsat 5 TM[J]. Sensor Letters, 2012, 10(1-2): 608-614.

[10] ZHENG Q, HUANG W, CUI X, et al. New spectral index for detecting wheat yellow rust using sentinel-2 multispectral imagery[J]. Sensors, 2018, 18(3): ID 868.

[11] HE L, QI S, DUAN J, et al. Monitoring of Wheat powdery mildew disease severity using multiangle hyperspectral remote sensing[J]. IEEE Transactions on Geoscience and Remote Sensing, 2020, 59(2): 979-990.

[12] ZHAO J, FANG Y, CHU G, et al. Identification of leaf-scale wheat powdery mildew (*Blumeria graminis* f. sp. *Tritici*) combining hyperspectral imaging and an SVM classifier[J]. Plants, 2020, 9(8): ID 936.

[13] KHAN I H, LIU H, LI W, et al. Early detection of powdery mildew disease and accurate quantification of its severity using hyperspectral images in wheat[J]. Remote Sensing, 2021, 13(18): ID 3612.

[14] ZHAO J, XU C, XU J, et al. Forecasting the wheat powdery mildew (*Blumeria graminis* f. Sp. *tritici*) using a remote sensing-based decision-tree classification at a provincial scale[J]. Australasian Plant Pathology, 2018, 47(1): 53-61.

[15] LIANG W, CARBERRY P, WANG G, et al. Quantifying the yield gap in wheat-maize cropping systems of the Hebei Plain, China[J]. Field Crops Research, 2011, 124(2): 180-185.

[16] CHEN H, ZHANG H, LI Y. Review on research of meteorological conditions and prediction methods of crop disease and insect pest[J]. Chinese Journal of Agrometeorology, 2007, 28(2): 212-216.

[17] YUAN L, PU R L, ZHANG J C, et al. Using high spatial resolution satellite imagery for mapping powdery mildew at a regional scale[J]. Precision Agriculture, 2016, 17(3): 332-348.

[18] LOVELAND T R, IRONS J R. Landsat 8: The plans, the reality, and the legacy[J]. Remote Sensing of Environment, 2016, 185: 1-6.

[19] WANG W, LIANG S, MEYERS T. Validating MODIS land surface temperature products using long-term nighttime ground measurements[J]. Remote Sensing of Environment, 2008, 112(3): 623-635.

[20] HUANG L, JIANG J, HUANG W, et al. Wheat yellow rust monitoring based on Sentinel-2 Image and BPNN model[J]. Transactions of the Chinese Society of Agricultural Engineering, 2019, 35(17): 178-185.

[21] LIU R, ZAHNG S, JIA R. Application of feature selection method in building information extracting from high resolution remote sensing image[J]. Bulletin of Surveying and Mapping, 2018, (2):126-130.

[22] BAO W, ZHAO J, HU G, et al. Identification of wheat leaf diseases and their severity based on elliptical-maximum margin criterion metric learning[J]. Sustainable Computing: Informatics and Systems, 2021, 30: ID 100526.

[23] QIN F, LIU D, SUN B, et al. Identification of alfalfa leaf diseases using image recognition technology[J]. PLoS One, 2016, 11(12): ID e0168274.

[24] ROBNIK-ŠIKONJA M, KONONENKO I. Theoretical and empirical analysis of ReliefF and RReliefF[J]. Machine Learning, 2003, 53(1): 23-69.

[25] JORDAN C F. Derivation of leaf-area index from quality of light on the forest floor[J]. Ecology, 1969, 50(4): 663-666.

[26] ROUSE J W, HAAS R H, SCHELL J A, et al. Monitoring vegetation systems in the great plains with ERTS[C]// In Third ERTS Symposium Volume 1: Technical Presentations. Washington, DC, USA: NASA, 1973: 309-317.

[27] GAMON J A, PNUELAS J, FIELD C B. A narrow-waveband spectral index that tracks diurnal changes in photosynthetic efficiency[J]. Remote Sensing of Environment, 1992, 41: 35-44.

[28] HUETE A R. A soil-adjusted vegetation index (SAVI)[J]. Remote Sensing of Environment, 1988, 25(3): 295-309.

[29] LIU H, HUETE A. A feedback based modification of the NDVI to minimize canopy background and atmospheric noise[J]. IEEE Transactions on Geoscience and Remote Sensing, 1995, 33 (2): 457-465.

[30] BROGE N H, LEBLANC E. Comparing prediction power and stability of broadband and hyperspectral vegetation indices for estimation of green leaf area index and canopy chlorophyll density[J]. Remote Sensing of Environment, 2000, 76(2): 156-172.

[31] RICHARDSON A J, WIEGAND C L. Distinguishing vegetation from soil background information[J]. Photogrammetric Engineering and Remote Sensing, 1977, 43(12): 1541-1552.

[32] PENUELAS J, BARET F, FILELLA I. Semi-empirical indices to assess carotenoids/chlorophyll a ratio from leaf spectral reflectance[J]. Photosynthetica, 1995, 31(2): 221-230.

[33] DU C, REN H, QIN Q, et al. A practical split-window algorithm for estimating land surface temperature from Landsat 8 data[J]. Remote Sensing, 2015, 7(1): 647-665.

[34] REN H, DU C, LIU R, et al. Atmospheric water vapor retrieval from Landsat 8 thermal infrared images[J]. Journal of Geophysical Research: Atmospheres, 2015, 120(5): 1723-1738.

[35] GAO F, MASEK J, SCHWALLER M, et al. On the blending of the Landsat and MODIS surface reflectance: Predicting daily Landsat surface reflectance[J]. IEEE Transactions on Geoscience and Remote Sensing, 2006, 44(8): 2207-2218.

[36] OLATOMIWA L, MEKHILEF S, SHAMSHIRBAND S, et al. A support vector machine-firefly algorithm-based model for global solar radiation prediction[J]. Solar Energy, 2015, 115: 632-644.

[37] HUANG L, LIU W, HUANG W, et al. Remote sensing monitoring of winter wheat powdery mildew based on wavelet analysis and support vector machine[J]. Transactions of the Chinese Society of Agricultural Engineering, 2017, 33(14): 188-195.

[38] MA H, HUANG W, JING Y. Wheat powdery mildew forecasting in filling stage based on remote sensing and meteorological data[J]. Transactions of the Chinese Society of Agricultural Engineering, 2016, 32(9): 165-172.

[39] XU H. Retrieval of the reflectance and land surface temperature of the newly-launched Landsat 8 satellite[J]. Chinese Journal of Geophysics-Chinese Edition, 2015, 58(3): 741-747.

[40] SHARMA A K, SHARMA R K, BABU K S, et al. Effect of planting options and irrigation schedules on development of powdery mildew and yield of wheat in the North Western plains of India[J]. Crop Protection, 2004, 23(3): 249-253.

联合多源多时相卫星影像和支持向量机的 小麦白粉病监测方法

赵晋陵¹, 杜世州^{2*}, 黄林生¹

(1. 安徽大学农业生态大数据分析与应用技术国家地方联合工程研究中心, 安徽合肥 230601;
2. 安徽省农业科学院 作物研究所, 安徽合肥 230031)

摘要: 白粉病主要侵染小麦叶部, 可利用卫星遥感技术进行大范围监测和评估。本研究利用多源多时相卫星遥感影像监测小麦白粉病并提升分类精度。使用四景 Landat-8 的热红外传感器数据 (Thermal Infrared Sensor, TIRS) 和 20 景 MODIS 影像的 MOD11A1 温度产品反演地表温度 (Land Surface Temperature, LST), 使用 4 景国产高分一号 (GF-1) 宽幅相机数据 (Wide Field of View, WFV) 提取小麦种植区和计算植被指数。首先, 利用 ReliefF 算法优选对小麦白粉病敏感的植被指数, 然后利用时空自适应反射率融合模型 (Spatial and Temporal Adaptive Reflectance Fusion Model, STARFM) 对 Landsat-8 LST 和 MOD11A1 数据进行时空融合。利用 Z-score 标准化方法对植被指数和温度数据统一量度。最后, 将处理和融合后的单一时项 Landsat-8 LST、多时相 Landsat-8 LST、累加 MODIS LST 和多时相 Landsat-8 LST 与累加 MODIS LST 结合的数据分别输入支持向量机 (Support Vector Machine, SVM) 构建了四个分类模型, 即 LST-SVM、SLST-SVM、MLST-SVM 和 SMLST-SVM, 利用用户精度、生产者精度、总体精度和 Kappa 系数对比四个模型的分类精度。结果显示, 本研究构建的 SMLST-SVM 取得了最高分类精度, 总体精度和 Kappa 系数分别为 81.2% 和 0.67, 而 SLST-SVM 则为 76.8% 和 0.59。表明多源多时相的 LST 联合 SVM 能够提升小麦白粉病的识别精度。

关键词: 小麦白粉病; 高分一号; MODIS; Landsat-8; 地表温度; 支持向量机

(登陆 www.smartag.net.cn 免费获取电子版全文)